

Surface Characterizations of Carbon Multiwall Nanotubes: Comparison between Surface Active Sites and Raman Spectroscopy

Cathie Vix-Guterl,^{*,†} Michel Couzi,[‡] Joseph Dentzer,[†] Michel Trinquescoste,[‡] and Pierre Delhaes^{*,‡}

Institut de Chimie des Surfaces et Interfaces (ICSI), CNRS, 15 rue Jean Starcky, 68057 Mulhouse Cedex, France, and Centre de Recherche Paul Pascal et Laboratoire de Physicochimie Moléculaire, CNRS et Université Bordeaux I, 33600 Pessac, France

Received: June 25, 2004; In Final Form: September 9, 2004

In carbon nanotubes and nanofilaments, the surface properties play a fundamental role for any use or application. It is therefore necessary to know and to control their surface characteristics, which are dependent on the fabrication process and surface treatments. In this work, two selected series of multiwalled nanotubes on which a thermal treatment and/or a controlled surface oxidation, using nitric acid solutions, have been carried out. The structural changes of the nanotubes due to these treatments have been followed by means of two different approaches: first, a solid-state chemistry approach with the determination of chemical surface properties of the carbon characterized by the active surface area (ASA) concept and, second, a more physical approach with Raman microspectroscopy. With this track, it was possible to quantify the surface/morphology ratio in nanotubes, especially in relation with their wettability and adhesion. Hence, we have established a general relationship between physical and chemical approaches that should be valid for any mesoporous, and even macroporous, carbons.

1. Introduction

The fundamental role played by the surface of carbon nanotubes and nanofilaments in any assembling system is not well elucidated yet. For a given volumetric fraction in a biphasic medium, the nanotube surface area is very large and the quality of its associated interfacial bonding is crucial to control the induced macroscopic physical properties.¹ As already demonstrated for the regular carbon fiber–polymer matrix composites, the wetting and adhesion characteristics have to be controlled for an optimized mechanical application or some other interfacial property.²

With this track, the starting point to consider is the graphene ideal plane that presents a weak energy surface due only to the dispersive term and associated hydrophobic character.³ In such a situation, a physisorption process with an organic compound will occur usually thanks to a π – π type interaction.⁴ Before the advent of nanotubes, the field of interfacial chemistry of carbon surfaces had been thoroughly developed with the concept of the active surface area (ASA)⁵ related to chemically accessible and reactive sites giving rise to the possibility of covalent bonding.⁶ Usually these reactive sites are located at the edges of the graphene planes (i.e., on the prismatic faces and inside the hexagonal network as point defects, vacancies, and dislocations). Their concentration in graphitic carbons is dependent upon the so-called crystallite size and associated bulk orientation, characteristics of the current structural order, which can be also studied by Raman microspectroscopy as explained later. The amount of active sites can be quantified by oxygen chemisorption as described in the Experimental Section. It has been shown

that this concept and the ASA quantification technique can be extended to characterize nanotubes.⁷ The so-called active sites are generally sites of higher surface energies and hence are easily oxidized, generating carbon–oxygen surface groups in particular for disordered graphitic carbons, which present lattice defects and dangling bonds.³ Different phase oxidation of carbon fibers has been found to be quite effective in modifying the surface chemistry of carbon, leading to improvements of the mechanical properties of carbon fiber–resin composites.² These liquid phase oxidations, as, for example, in diluted nitric acid, are milder compared to the gaseous phase treatments as plasma treatment, and generally they do not cause excessive pitting and degradation of the filaments. However, a treatment with concentrated nitric acid could damage their texture and will induce a decrease in the physical properties.⁸ Oxidation with nitric acid results in the formation of considerable amounts of functional groups, such as carbonyl (–COOH) and hydroxyl (–OH) groups, which induce a modification of the surface polarity.⁹ The heterogeneous carbon surface also becomes partially hydrophilic; after excessive oxidation, this hydrophilic character will win over the initial hydrophobic one, then high sorption of water is even observed.¹⁰ To our knowledge, no particular attention has been paid so far to the treatment of carbon nanotubes with nitric acid with the objective to control their surface chemistry (and not to purify them) and consequently to modify their interfacial properties without altering their bulk texture.

It turns out that the control of the carbon surface chemistry is a key parameter that we decided to study on two series of multiwall carbon nanotubes (MWNTs) grown by catalytic chemical vapor deposition (CVD), also called vapor grown carbon fibers (VGCFs).¹¹ We have modulated the surface characteristics by different thermal or chemical treatments, as presented in the following Experimental Section. The changes of the surface chemistry are followed by the measurement of the

* Authors to whom correspondence should be addressed. E-mail: C.Vix@uha.fr; delhaes@crpp-bordeaux.cnrs.fr.

[†] Institut de Chimie des Surfaces et Interfaces (ICSI).

[‡] Centre de Recherche Paul Pascal et Laboratoire de Physicochimie Moléculaire.

TABLE 1: Structural Characterization of Nanofilaments Samples

| nanofilamentous samples | weight loss % | filaments diameter (nm) | | X-ray diffraction | | He density |
|--|---------------|-------------------------|------------------|-------------------|---------|-------------------|
| | | D_{ext} | D_{int} | d_{002} (nm) | Lc (nm) | |
| Multiwall Nanotubes Herringbone Form | | | | | | |
| as deposited | | 80 | 20 | 0.343 | 6.2 | 2.32 ^a |
| HNO ₃ treated | 7 | 80 | 15 | 0.342 | 6.3 | 2.11 |
| HTT = 2500 °C | 15 | 80 | 15 | 0.341 | 7.4 | 2.07 ^a |
| HTT + HNO ₃ treated | 3.5 | | | 0.339 | 7.7 | 2.20 |
| Multiwall Nanotubes Concentric Form Pyrograf III | | | | | | |
| as deposited | | 180 | 60 | 0.340 | 10.0 | 1.98 |
| HNO ₃ treated | 20 | 170 | 80 | 0.339 | 11.4 | 2.10 |
| HTT = 2500 °C | 4 | 150 | 80 | 0.338 | 12.5 | 2.07 |
| HTT + HNO ₃ treated | 0 | 140 | 65 | 0.337 | 12.8 | 2.20 |
| HTT + concentrated HNO ₃ treated | 21 | 140 | 70 | 0.338 | 11.1 | |

^a Density decrease due to catalyst vaporization.¹⁴

amount of oxygen functional groups present at the carbon surface as well as the evolution of the amount of active sites. The quantitative determination of the amount of functional groups at the carbon surface can be achieved by a temperature-programmed desorption procedure and the measurement of the ASA concentration by oxygen chemisorption.²

Raman spectroscopy is a powerful physical technique fully developed to characterize carbon materials.¹² This spectroscopy, as a witness of the crystallization process, has become, over these last years, more powerful than classical X-ray diffraction for poorly graphitized carbons. In particular, the determination of the carbon in-plane crystallite size, related to the structural order, is possible, associated with the appearance of several new bands when some lattice disorder is present in the crystal structure of hexagonal graphite. This nondestructive technique is also sensitive to the surface modifications occurring, for example, during some electrochemical treatments of fibers.¹³ The associated morphology change of these nanotubes following thermal and acid treatments also will be observed by transmission electron microscopy (TEM) as presented in the next paragraph. Finally in the last paragraph, we present evidence of a correlation between the physical and chemical approaches by assuming that the lattice defects quantitatively measured by Raman spectroscopy and oxygen chemisorption have a common origin. This correlation led us to a better knowledge and understanding of the surface and interface characteristics in these carbon multiwall nanotubes. This study is focused therefore on a double goal: (a) the control of the surface chemistry of carbon nanotubes by thermal and nitric acid treatments as followed by ASA measurements and Raman spectroscopy experiments, (b) the establishment of a relationship between these two different characteristics.

2. Experimental Results

Sample Characterizations. Two series of catalyzed CVD nanotubes were selected. The first one, prepared at 600 °C with a nickel catalyst, is characterized by its mean outside diameter around 70 nm with a “herringbone” morphology of the graphene sheets, as already shown on TEM micrographs.¹⁴ The second series is a classical VGCF prepared at low temperature with an iron-based catalyst and commercialized under the trade name Pyrograf III. The inner part of Pyrograf III consists mainly of slightly conical graphene layers with a mean total diameter up to 200 nm and a large internal hole (see Table 1). It appears that the nanotubes are covered by a layer of pyrocarbon as observed in Figure 1a. These purified samples have been graphitized by heat treatment (HTT) at 2500 °C for 90 min in a graphite furnace under inert atmosphere, leading to an increase in the structural ordering of the carbon as observed by

comparison between Figure 1, parts a and b. Besides, for both pristine and graphitized nanotubes, the influence of a chemical oxidation has been studied following a classical wet method using nitric acid as an oxidative agent.¹⁵ The samples have been cured for 48 h in a 2 M HNO₃ solution at 110 °C. In one case for the graphitized VGCF, a concentrated HNO₃ solution (60% in volume) has been used during 2 h. As already mentioned,¹⁶ the oxidation with concentrated nitric acid can damage the nanotubes thanks to some exfoliation process as shown from TEM observations presented in Figure 1c. All of the structural characteristics using classical X-ray diffraction together with the morphological observations from TEM experiments associated with true density obtained by helium pycnometry and weight losses due to the treatments are gathered in Table 1. From these results, two main points of information are relevant.

(a) Both the influences of thermal and chemical treatments are accompanied by a weight loss. During HTT, the impurities, in particular the catalyst residue as already demonstrated by magnetic measurements, helium density changes, and transmission electron microscopy, are eliminated.¹⁴ The chemical attack by dilute acid concerns the more amorphous parts with the formation of surface acidic groups^{3,9} without any significant change in the nanotube diameters. Moreover, it can be observed that the weight loss after treatment by dilute nitric acid is much lower with the high-temperature-treated samples than the pristine samples.

(b) The pristine herringbone nanotubes made with quasi-planar sheets appear a little more ordered than the as-deposited Pyrograf III, as indicated by the comparison of the values of the mean interlayer spacing d_{002} and Lc, which corresponds to the coherence length perpendicular to the graphene planes, which were determined from the classical Scherrer relation applied to the diffraction line width. This has been also confirmed by TEM observations as already mentioned.¹⁴ This effect is reversed, however, after graphitization because the most concentric graphene layers can be more developed in length (as characterized by the in-plane coherence length L_a that we will discuss later). Nevertheless because of the geometrical constraints due to the atomic plane curvatures, this graphitization effect is not fully achieved; indeed the d_{002} interlayer spacing does not reach the classical value for a fully graphitized sample.

Surface Properties and Microtexture of MWNTs. The surface chemical characteristics of these MWNTs have been characterized as already introduced.¹⁵ The total surface area (TSA), implying mainly the basal planes, has been determined thanks to the classical BET method by physisorption on nitrogen at 77 K. The micropore volume has been determined from CO₂ adsorption at 273 K. Although the dimension of a CO₂ molecule is similar to that of N₂, the higher adsorption temperature results

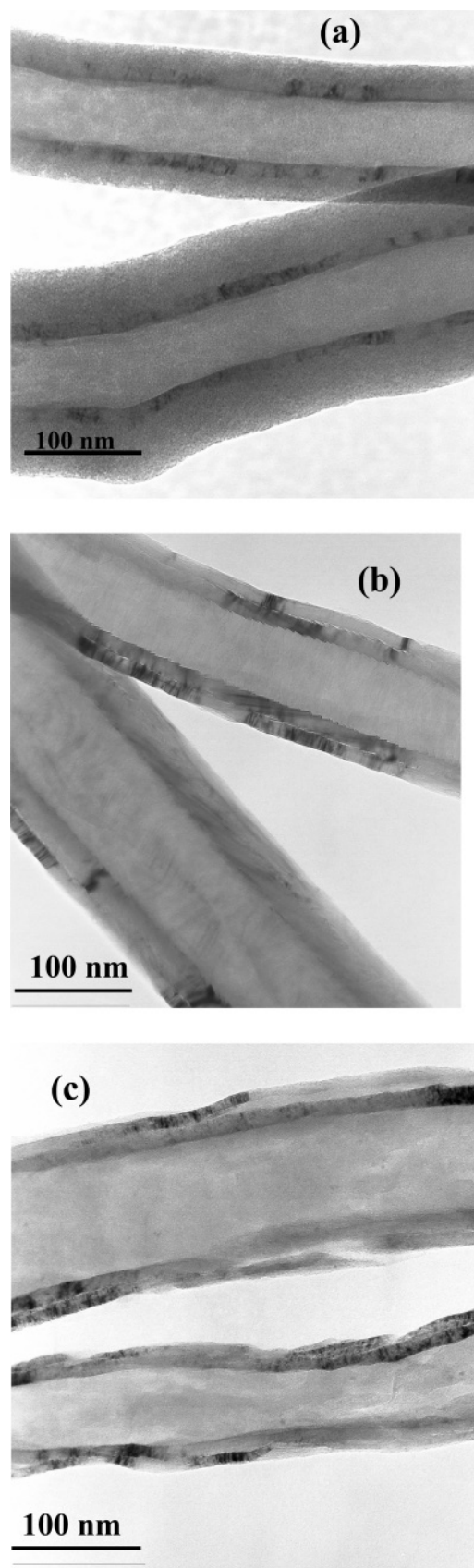


Figure 1. TEM pictures of Pyrograph III: (a) a graphitized sample and (b) the same sample after concentrated HNO_3 oxidation.

in better diffusion inside the narrowest micropores (size of the pores smaller than 0.7 nm). The micropore volume is calculated according to the usual Dubinin–Radushkevitch equation.¹⁷ The nature and the amount of the oxygen complexes chemisorbed

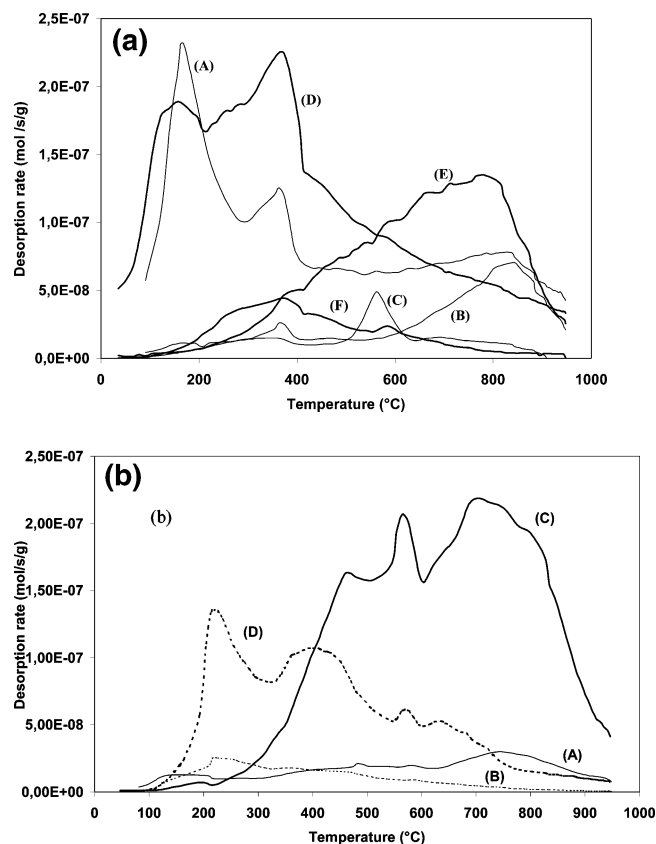


Figure 2. (a) Gas evolution during TPD of a Pyrograph III sample before and after nitric acid treatment: (A) H_2O , (B) CO , (C) CO_2 (before HNO_3 treatment), (D) H_2O , (E) CO , (F) CO_2 (after HNO_3 treatment). (b) Gas evolution during TPD of a Pyrograph III sample after oxidation in diluted and concentrated nitric acid: (A) CO , (B) CO_2 (sample oxidized in diluted HNO_3), (C) CO , (D) CO_2 (sample oxidized in concentrated HNO_3).

during the nitric acid oxidation on the edges of carbon atoms, which are thermally unstable, can be determined by thermal-programmed desorption (TPD).³ The TPD technique was performed in a vacuum system equipped with a mass spectrometer at a maximum pressure of 10^{-4} Pa. The graphite sample was deposited in a fused silica tube and heat-treated up to 1000 °C with a linear heating rate of 10 °C/min. During the experiment, the exhaust gas phase was quantitatively analyzed by mass spectrometry. As an illustration, the TPD diagrams (desorption rates of CO , CO_2 , and H_2O gases are recorded as a function of decomposition temperature obtained for the Pyrograph III sample before and after nitric acid treatment) are represented in Figure 2. In general, CO_2 is appearing at lower temperatures than CO and has been attributed to the decomposition of carboxylic, anhydride, or lactone groups. Besides, CO desorption takes place at a higher temperature than the decomposition of groups such as phenol, carbonyl, quinone, ether, and pyrene. Cyclic anhydrides of carboxylic acids produce CO and CO_2 in thermal decomposition.^{3,18–21} The total amount of each gas evolved during the TPD can be calculated by integrating the TPD curves as reported in Table 2 for almost all of the samples. Then the active surface area (ASA), corresponding mainly to edge planes and defects, has been measured using the established procedure. After the material was outgassed at 950 °C under vacuum, an initial oxygen pressure of 66.5 Pa is introduced in the reactor at 300 °C leading to the formation of surface oxygen complexes at a specific part of the graphite surface. The amount of oxygen complexes formed was determined by measuring the amount of CO and

TABLE 2: Surface Properties of Pristine and Treated Nanotubes

| nanofilamentous samples | TSA ^a (m ² g ⁻¹) | ASA ^b (m ² g ⁻¹) | $d_{\text{ASA}} = \text{ASA/TSA}$ | surface groups ($\mu\text{mol g}^{-1}$) | | | |
|--|--|--|-----------------------------------|---|------------------|-----|-----------------|
| | | | | H ₂ | H ₂ O | CO | CO ₂ |
| Multiwall Nanotubules Herringbone Form | | | | | | | |
| as deposited | 85 | 8 | 0.10 | 180 | 620 | 790 | 290 |
| HNO ₃ treated | 134 | 27 | 0.19 | — | — | — | 330 |
| HTT = 2500°C | 72 | 0.2 | 0.03 | 8.4 | 25 | 4.6 | 2.6 |
| HTT + HNO ₃ treated | 64 | 12 | 0.19 | 130 | 2.6 | 180 | 30 |
| multiwall nanotubules concentric form Pyrograf III | | | | | | | |
| as deposited | 34 | 3.2 | 0.09 | 1700 | 550 | 170 | 68 |
| HNO ₃ treated | 85 | 22 | 0.26 | 300 | 670 | 390 | 98 |
| HTT = 2500°C | 15 | 0.9 | 0.06 | 160 | 380 | 72 | 24 |
| HTT + HNO ₃ treated | 38 | 2.0 | 0.05 | 180 | 320 | 150 | 62 |
| HTT + concentrated HNO ₃ treated | 65 (600°) | 15.0 | 0.26 | 250 | 810 | 640 | 290 |

^a TSA = total surface area. ^b ASA = active surface area. ^c BET from CO₂ adsorption and total amount of H₂, H₂O, CO, and CO₂ desorbed during the TPD experiment.

CO₂ desorbed from the carbon sample at a temperature higher than the complex formation temperature by performing a temperature-programmed desorption analysis between 350 and 950 °C. With the number of moles of each desorbed gas and the area of an edge carbon site that chemisorbed an oxygen atom as 0.0083 nm², the surface area occupied by chemisorbed oxygen can be determined.^{5,22}

As shown in Table 2, a decreased amount of gases desorbed from the surface of the nanotubes is observed after heat treatment at 2500 °C. This is also reflected in the values of ASA and d_{ASA} , where d_{ASA} is defined as the ratio between ASA and TSA values. In a classical case, this ratio furnishes an estimate of the ratio between the edge and plane surfaces and should be related with the mean crystallite size. As expected, the experimental results indicate that the heat treatment of the nanotubes leads to a significant increase in the structural ordering of the carbon as already confirmed by TEM (Figures 1). The annealing of the structural defects during the heat treatment leads to the development of a very homogeneous surface essentially composed of basal planes as confirmed by the very low d_{ASA} values.

The effect of the modification of carbon surface chemistry by the HNO₃ oxidation can be clearly observed in Figure 2 and is summarized in Table 2. As indicated by the gas profile in Figure 2, the oxygen-containing surface complexes present on HNO₃-oxidized carbons desorbed during TPD can be divided into four distinct groups, the lower- and higher-temperature CO₂-yielding surface complexes and the lower- and higher-temperature CO-yielding surface complexes. The oxygen groups are essentially completely decomposed by heat treatment to 900 °C. As seen in Table 2, the acid treatment leads to a significant increase in the amount of H₂O, CO, and CO₂. Generally, the wet oxidation of a carbon material leads to an increase in the quantity of CO₂ evolved, much more important than in the case of air or oxygen oxidation. This is due to the fact that the carboxyl groups created at low temperatures during HNO₃ decomposed already below 300 °C. Above this temperature, the CO₂ and CO (at higher temperature) desorption are attributed to the decomposition of lactone groups created during HNO₃ treatment and, to some extent, originated during heating rearrangements. The CO evolution at temperatures higher than 550 °C corresponds to the decomposition of the more thermally stable phenol or ether groups.^{18,21} After acid treatment, it was also observed that H₂O desorbed up to 400 °C; this large amount is attributed to the elimination of acidic oxygen complexes and to a partial transformation of these groups (e.g., condensation of any adjacent phenolic or carboxylic acid groups present at the surface). It must be noted that the

nitric acid oxidation not only introduces oxygen complexes but also results in a significant quantity of nitro groups via the nitration mechanism.²³

The presence of increased numbers of functional groups is relevant to the formation of structural defects during the nitric acid oxidation, as confirmed by the measured ASA values. The wet oxidation affects not only the surface chemical composition but also the texture as indicated by the increased TSA value.

The quantities of H₂O, CO, and CO₂ increase significantly with the nitric acid concentration. This is in agreement with the measured ASA and TSA values. The significant micropore volume determined by CO₂ adsorption indicates that the wet-oxidation process with concentrated nitric acid induces the formation of an important narrow microporosity (pore size less than 0.7 nm) not observed after oxidation with diluted nitric acid. Such phenomena were already noted with regular carbon fibers.¹⁵

From all these data given, we deduce several facts, starting from TSA values which are decreasing with thermal treatments and increasing under nitric acid attacks. These areas can be compared with the external geometrical surface calculated for concentric nanotubes,²⁴ the estimated surfaces are 25 and 13 m² g⁻¹ for the two considered series, respectively. We see immediately that the BET value obtained for graphitized Pyrograf III only is in good agreement. For the other samples, the extra surfaces are related to structural imperfections and microporosities, in particular after concentrated HNO₃ oxidation. Concerning the ASA values, we observe larger values for the MWNT presenting a fishbone morphology than those for Pyrograf III ones, with a strong decrease after graphitization and a large increase under oxidation for both series. Indeed, it can be observed by TEM that the graphitized Pyrograf III are made of almost perfect concentric nanotubes. In this case, the ASA content should be almost zero in absence of any graphite edge except at the caps. We can see in Table 2 that the ASA value is higher than that for the herringbone nanotubes; this is attributed to the presence of the pyrocarbon deposit (Figure 1a) which is less organized than the internal part. Therefore, the experimental results show the influences of both different morphologies and surface treatments on the presence of active sites. It must be noticed that the density (d_{ASA}) values are increasing more than those obtained for a regular burnoff,^{2,5} showing that the defects located in both basal surfaces and edges are increasing simultaneously, as we will investigate physically now.

Raman Spectroscopy and MWNT Characterization. As indicated in the Introduction, we will start from ideal graphite Raman spectra.¹² It has been observed in highly oriented

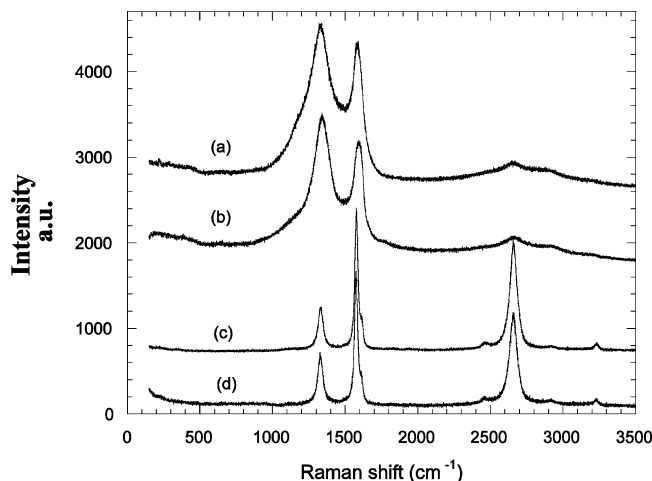


Figure 3. Raman spectra of selected Pyrograf III MWNT: (a) pristine sample, (b) pristine sample after 2 M HNO₃ oxidation, (c) after graphitization (HTT = 2500°), (d) after graphitization and oxidation by concentrated HNO₃.

pyrolytic graphite (HOPG) that only two modes are active, the E_{2g} modes, respectively, at 42 and 1580 cm⁻¹ (the so-called G band), together with second-order features, in particular one intense band around 2700 cm⁻¹. The first-order spectrum of microcrystalline graphite shows additional bands around 1350 and 1620 cm⁻¹ called D and D' bands, respectively, due to the presence of lattice defects and the loss of the long-range in-plane symmetry which release the usual selection rule.²⁵ In the literature, there are several examples of loss of the hexagonal symmetry, in the case of implanted ions, neutron irradiated,²⁶ or boron doped HOPG²⁷ with evidence of defects at the graphite edge planes associated with the D line.²⁸ These observations have been extended to all the graphitic forms of carbons.^{29,30} As proposed more than 20 years ago by Tuinstra and Koenig,³¹ a relationship can be established between the intensity ratio of the D and G bands ($R = I_D/I_G$) and the inverse of the in-plane coherence length (L_a), which is the mean crystallite size. Later, it was shown that the intense D mode depends on the laser excitation wavelength; this dispersive behavior is related with a resonant scattering process, and the ratio R is dependent on the frequency of the exciting light.³² It has been demonstrated furthermore that the second-order line located at 2700 cm⁻¹ (2D harmonic mode) is also dispersive with a laser energy slope dependence twice that of the D line variation.³³ Finally, it turns out that the electronic dispersion in graphite gives rise to a specific double resonant process for these lines.³⁴ These results point out that all of the experiments on different samples have to be carried out at a fixed laser frequency for a direct comparison between them.

In this series of experiments, we have worked with a Jobin–Yvon microspectrometer fitted with an He–Ne laser at $\lambda = 632.8$ nm; the laser spot on the samples is around 1 μm^2 with an incident power no higher than 1 mW to prevent any sample heating. Typical spectra recorded for Pyrograf III samples are presented in Figure 3 where we observe that both the chemical oxidation and the thermal treatment modify the full spectra but not the band positions. The Raman spectra of pristine and posttreated herringbone type carbon nanotubes already have been reported;¹⁴ they are quite similar to the spectra shown in Figure 3. We have also checked that the Raman characteristics obtained after the surface property measurements are almost unchanged, for clarity they are not given in Table 3.

To analyze these differences, we have reported in Table 3 the respective line widths and the intensity ratios, $R = I_D/I_G$

and $R' = I_{2D}/I_G$, obtained from integrated areas. In this table, we have indicated the results obtained with an HOPG sample used as reference with the G and 2D bands located at 1580 and 2685 cm⁻¹, respectively (the D band is detected for these nanotubes in the range 1330–1340 cm⁻¹). We detect a line width narrowing after graphitization, mainly observed on Pyrograf III; indeed these pristine and oxidized MWNTs exhibit very broad G and D lines, which seem related to the graphene planes' curvature and the associated stress as seen on other noncrystalline carbons exhibiting a specific line broadening.³⁵ This point is confirmed by the line width comparison between G and D lines and the second-order one (2D),³⁶ which is almost double in all the cases, except for the pristine Pyrografs III. After HTT at 2500 °C, these stresses are released, and a line width narrowing is observed that does not reach completely the graphite value. As already demonstrated, there is a relationship between this physical quantity and the degree of graphitization,³³ which is only partial for these samples (see the d_{002} values reported in Table 1 which are always larger than those for the Pyrographite HOPG). Here, the respective intensity ratio R was determined by using the following relation

$$R(\lambda) = \frac{I_D}{I_G} = \frac{C(\lambda)}{L_a} \quad (1)$$

with $C(\lambda) = 8.28$ nm for $\lambda = 632.8$ nm. This relation, valid for $L_a > 2$ nm,²⁶ leads to the determination of the in-plane correlation lengths L_a given in Table 3. After heat treatment at 2500 °C, we observe immediately a simultaneous decrease of R together with an increase of R' characteristic of L_a growing, as presented in Figure 4. For these microcrystalline samples, the intensity of the “forbidden” D line, associated with defects inside the aromatic rings, is disappearing while the mean graphitic crystallite size is growing. But during the same time the second-order light scattering, which does not need defects to be Raman active because it involves two identical phonons with opposite wave vectors, is strongly favored²⁹ as observed for similar graphitized nanofilaments.³⁷ It is interesting to see a regime change for L_a larger than 10 nm and corresponding to a crystallite volume around 1000 nm² (with L_c about 10 nm for the graphitized nanotubes, Table 1). We can consider in first approximation that both the phonon and the electron spectra are reaching a very similar step compared to the single-crystal ones.^{12,25}

3. Comparative Analysis of the Surface Characterizations

Relationship between the Amount of Active Sites and the In-Plane Correlation Length. We have seen that the ASA concept is related to the carbon surface chemical properties,⁶ indicating currently the presence of oxygen functional groups as given by TPD experiments (Figure 2). This parameter is more significant than the TSA values that give the accessible surface under given experimental conditions. (We have seen in one case that N₂ and CO₂ adsorptions are furnishing different results.) In the case of tubular shape, there is no real graphitic edges but rather planar defects that we can relate to L_a , the correlation length seen as a mean interdefect distance. In Figure 5a, the log–log plot of ASA versus L_a has been represented, determined from Raman scattering experiments. We observe an approximate linear relation with a slope around 1.8, which is confirmed by the regular plot shown in Figure 5b. The established following equation

$$\log\{\text{ASA}\} = 200 - 1.8 \log(L_a) \quad (2)$$

TABLE 3: Raman Data on the Two Series of MWNT and the HOPG Reference

| nanofilamentous samples | first order | | | | second order | |
|--|---------------------------------------|---------------------|---------------|---------|---------------------------------------|-------------------|
| | $\Delta\nu_{1/2}$ (cm ⁻¹) | | $R = I_D/I_G$ | La (nm) | $\Delta\nu_{1/2}$ (cm ⁻¹) | |
| | D line ^a | G line ^a | | | 2D line ^a | $R' = I_{2D}/I_G$ |
| Multiwall Nanotubes Herringbone Form | | | | | | |
| as deposited | 60 | 60 | 1.90 | 4.3 | 90 | 0.55 |
| HNO ₃ treated | 55 | 50 | 2.15 | 3.8 | 90 | 0.75 |
| HTT = 2500 °C | 35 | 35 | 0.50 | 16.5 | 60 | 1.30 |
| HTT + HNO ₃ treated | 40 | 30 | 0.90 | 9.2 | 55 | 1.60 |
| Multiwall Nanotubes Concentric Form Pyrograf III | | | | | | |
| as deposited | 130 | 75 | 1.50 | 5.5 | 125 | 0.25 |
| HNO ₃ treated | 140 | 85 | 2.10 | 4.0 | 130 | 0.20 |
| HTT = 2500°C | 40 | 25 | 0.30 | 27.5 | 50 | 1.50 |
| HTT + HNO ₃ treated | 40 | 30 | 0.50 | 16.0 | 50 | 1.40 |
| HTT + concentrated HNO ₃ treated | 50 | 30 | 0.80 | 9.0 | 65 | 1.30 |
| HOPG Crystal (La > 100 nm) | | | | | | |
| | 13 | 25 | | 1.64 | | |

^a Raman lines.

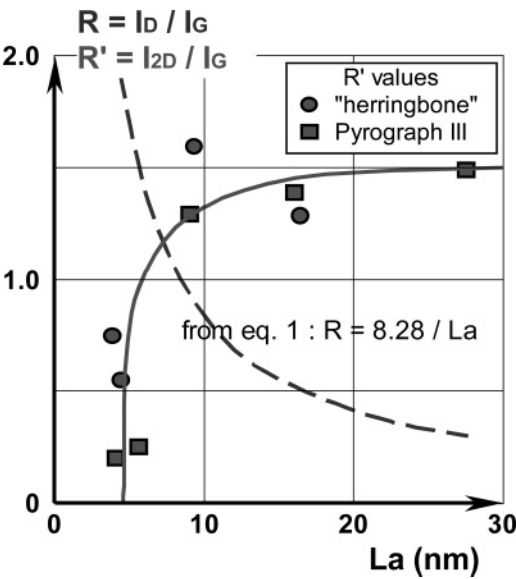


Figure 4. Raman intensity ratios (R and R') versus in-plane crystallite size (La) for both series of MWNTs.

is giving an empirical relationship between the two parameters. We can notice that for $La = 1$ nm, $\{ASA\}_0 = 200$ m²/g, a rather high value which could be interpreted as the optimal edge surface as already found in active carbons with superhigh surfaces.³⁸ As $\{ASA\}$ is homogeneous to a surface and La is a characteristic length, we should observe rather a square dependence between them. In fact during the Raman experiments, the laser electromagnetic wave is penetrating with a skin depth around 50 nm and an exponential amplitude decrease, reaching almost all the individual nanotubes and integrating all the structural defects. It is known, from TEM observations, for example,³⁹ that the density of surface defects, forming craters or dislocations including several graphitic planes on the skin, is pertinent. We assume therefore that the Raman spectra, which are also integrating the more regular internal layers, are giving rise to a weaker exponent value ($n = 1.8$), representative nevertheless of the density of surface defects detected by the ASA technique, as given by eq 2. The most drastic departure is after concentrated nitric acid attack, with a rather large mass loss (Table 1), where the surface activation is giving rise to a new microporosity that is not sensitive to Raman spectra. As pointed out by Lahaye,⁴⁰ this is a specific behavior of microporous carbons which is not detected by Raman spectroscopy

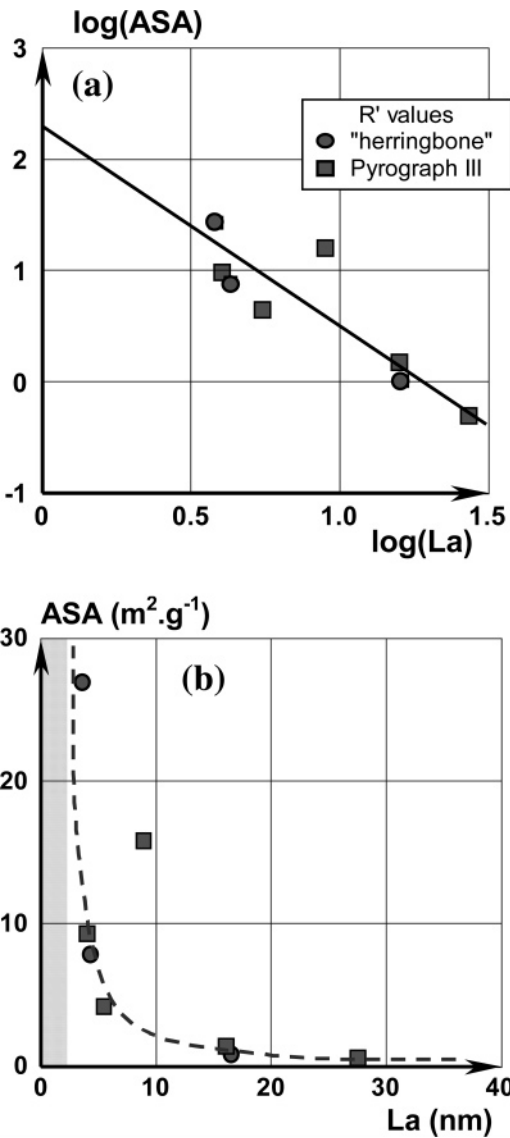


Figure 5. Active surface area (ASA) versus in-plane crystallite size (La): (a) in log–log scale with the established relation given in the text, (b) in linear scale with the dashed zone ($La < 2$ nm) where the La calculation is nonvalid.

because we have noted that eq 1 is valid for $La > 2$ nm. (See the experimental points in Figure 5b which present the highest ASA values in the presence of microporosities.)

Graphene Interfacial Behavior. The interfacial characteristics of nanotubes are related with both their surface quality and subsequent functionalization. As we have measured it, the density of ASA can reach around 20–25% of the total surface, as shown in Table 2 with the d_{ASA} ratio. This optimized value is larger than that found in classical carbon fibers,² and the initial hydrophobic character, which is even reinforced by the increase of surface roughness,⁴¹ should become hydrophilic with the increase of surface coverage by several types of acidic and hydroxyl groups as it could be supposed in a kind of a 2D percolation system.⁹ This point is crucial for a good wettability and the associated work of adhesion inside a composite material as expected from preliminary wettability experiments. After graphitization, we are in the presence of an “ideal” graphene surface with a low energy, and the nanofiber–matrix adhesion is governed by a physisorbed reversible mechanism that can be efficient with alkyl chains or polyaromatics as demonstrated by AFM observations⁴² and developed for gas sensor use.⁴³ At the opposite in the presence of chemical active surface groups, covalent bonds can be created at the interface, and the level of fiber–matrix adhesion is reinforced for mechanical properties thanks to the increase in interfacial shear strength² but not really proved in the case of nanotubes. It appears indeed that the control of the ASA value is a key parameter that indicates the kind of preferred interfacial interaction, which ultimately depends on the type of combined property and forecasted application.

4. Conclusion

We have established a relation between a surface chemical analysis and a spectroscopic property on two series of different carbon nanotubes. This relation can be extended to other nanofilaments⁶ as far as the mesoporosities are involved but not the microporosities in these multiscale materials. The thermal and chemical treatments are able to modify the heterogeneous graphene surfaces, in particular it would be interesting to compare the influence of different oxidations using either a dry (plasma) or a wet (electrooxidation) oxidation and subsequently the type of functional groups which will give rise to a specific covalent bonding.

We have shown that the in-plane correlation length (L_a) is decreasing after a chemical oxidation. It is well-known that the mechanical properties, in particular the classical YOUNG modulus, are inversely proportional to L_a (and their crystallite spatial distribution) for all the carbon filaments.⁴⁴ The final performance of a nanocomposite is determined by the compromise between the intrinsic properties of the nanoreinforcement and its interfacial shear strength with a given matrix. With this point in mind, a careful control of the surface properties is necessary to optimize the functionalization process without any real degradation of the bulk nanotubes. As an alternative, noncovalent bonding appears promising because it does not damage the original π -networks and the associated properties⁴² and is a promising way for actuator and sensor devices with reversible mechanism as gas or vapor capture.

Acknowledgment. The authors acknowledge Dr. L. Vidal for his technical help in TEM experiments.

References and Notes

(1) Baughman, H.; Zakhidov, A. A.; De Heer, W. A. *Science* **2002**, 297, 78.

- (2) Vix-Guterl, C.; Ehrburger, P. *Fibers and Composites: World of Carbon*; Taylor and Francis: London and New York, 2003.
- (3) Boehm H. P. *Graphite and Precursors: World of Carbon*; Gordon and Breach: London and New York, 2001.
- (4) Star, A.; Liu, Y.; Grant, K.; Stoddart, J. F.; Steuerman, D. W.; Diehl, M. R.; Boukai A.; Heath, J. R. *Macromolecules* **2003**, 36, 553.
- (5) Laine, R. N.; Vastola F. J.; Walker P. L. *J. Phys. Chem.* **1963**, 67, 2030.
- (6) Leon y Leon, C. A.; Radovic L. R. *Chemistry and Physics of Carbon*; Marcel Dekker, Inc.: New York, 1994; Vol. 24.
- (7) Vix-Guterl, C.; Dentzer, J.; Ehrburger, P.; Metenier, K.; Bonnamy S.; Beguin, F. *Carbon* **2001**, 39, 318.
- (8) Pittman, C. U., Jr.; Wu, Z.; Jiang, W.; He, G. R.; Wu, B.; Li W.; Gardner S. D.; *Carbon* **1997**, 35, 929.
- (9) Donnet, J.-B.; Brendle, M.; Dhami, T. L.; Bahl, O. P. *Carbon* **1986**, 24, 757.
- (10) Glaser, R.; Wietkamp J. *Handbook of Porous Solids*; Wiley-VCH: Germany, 2002; Vol. 2.
- (11) Tibbetts, G. G.; Doll, G. L.; Gorkiewicz, D. W.; Moleski, J. L.; Perry, T. A.; Dash C. J.; Balogh M. J. *Carbon* **1993**, 31, 1039.
- (12) Eklund, P. C.; Holden, J. M.; Jishi, R. A. *Carbon* **1995**, 33, 959.
- (13) Liu Y.-C.; McCreery, R. L. *J. Am. Chem. Soc.* **1995**, 117.
- (14) Cui, S.; Canet, R.; Derré, A.; Couzi M.; Delhaès, P. *Carbon* **2003**, 41.
- (15) Pamula, E.; Rouxhet, P. G. *Carbon* **2003**, 41, 1905.
- (16) Jia, Z.; Wang, Z.; Liang, J.; Wei B.; Wu, D. *Carbon* **1999**, 37, 903.
- (17) Rodriguez-Reinoso, F.; Linares-Solano, A. In *Chemistry and Physics of Carbon*; Thrower, P. A., Ed.; Marcel Dekker: New York, 1989; Vol. 21, pp 1–146.
- (18) Otake, Y.; Jenkins, R. G. *Carbon* **1993**, 31, 109.
- (19) Roman-Martinez M. C.; Cazorla-Amoros D.; Linares-Solano A.; Salinas-Martinez de Lecea, A. *Carbon* **1993**, 31, 895.
- (20) Tremblay, G.; Vastola, F. J.; Walker, P. L., Jr. *Carbon* **1978**, 16, 35.
- (21) de la Puente G.; Pis, J.J.; Menendez, J. A.; Grange P. *J. Anal. Appl. Pyrolysis* **1997**, 43, 125.
- (22) Harat, P. J.; Vastola, F. J.; Walker, P. L., Jr. *Carbon* **1967**, 5, 363.
- (23) Salame, I. I.; Bandosz T. J. *J. Colloid Interface Sci.* **2001**, 240, 252.
- (24) Peigney, A.; Laurent, Ch; Flahaut, E.; Bacsa R. R.; Rousset, A. *Carbon* **2001**, 39, 507–514.
- (25) Ferrari A. C.; Robertson, J. *Phys. Rev. B* **2000**, 61, 14095.
- (26) Elman, B. S.; Shayegan, M.; Dresselhaus, M. S.; Mazurek H.; Dresselhaus, G. *Phys. Rev. B* **1982**, 25, 4142.
- (27) Hagio T.; Nakamizo, M.; Kobayashi, K. *Carbon* **1989**, 27, 259.
- (28) Compagnini, G.; Puglisi O.; Foti, G. *Carbon* **1997**, 35, 1793.
- (29) Nemanich R. J.; Solin, S. A. *Phys. Rev. B: Condens. Matter Mater. Phys.* **1979**, 20, 392.
- (30) Ferrari, A. C.; Robertson, J. *Phys. Rev. B: Condens. Matter Mater. Phys.* **2001**, 64, 1.
- (31) Tuinstra, F.; Koenig, J. L. *J. Chem. Phys.* **1970**, 53, 1126.
- (32) Pocsik, I.; Hundhausen, M.; Koos M.; Ley, L. *J. Non-Cryst. Solids* **1998**, 227–230B, 1083.
- (33) Matthews, M. J.; Pimenta, M. A.; Dresselhaus, G.; Dresselhaus, M. S.; Endo, M. *Phys. Rev. B: Condens. Matter Mater. Phys.* **1999**, 59, R6585.
- (34) Thomson, C.; Reich, S. *Phys. Rev. Lett.* **2000**, 85, 5214.
- (35) Schwan, J.; Ulrich, S.; Batori, V.; Ehrhardt, H.; Silva, S. R. P. *J. Appl. Phys.* **1996**, 80, 440.
- (36) Lespade, P.; Marchand, A.; Couzi, M.; Cruège, F. *Carbon* **1984**, 22, 375.
- (37) Endo, M.; Kim, Y. A.; Takeda, T.; Hong, S. H.; Matusita, T.; Hayashi, T.; Dresselhaus, M. S. *Carbon* **2001**, 39, 2003–2010.
- (38) Kaneko, K.; Ishi, C.; Ruike, M.; Kuwabara, H. *Carbon* **1992**, 30, 1075.
- (39) Andrews, R.; Jacques, D.; Quian, D.; Dickey, E. C. *Carbon* **2001**, 39, 1681.
- (40) Lahaye J. *Fuel* **1998**, 77, 543.
- (41) Li, S.; Li, H.; Song, X.; Liu, Y.; Jiang, L.; Zhu, D. *J. Phys. Chem. B* **2002**, 106, 9274.
- (42) Pécastaings, G.; Delhaès, P.; Derré, A.; Saadaoui, H.; Carmona, F.; Cui, S. *J. Nanosci. Nanotechnol.* **2004**, 4, 838.
- (43) Valentini, L.; Bavastrello, V.; Stura, E.; Armentano, I.; Nicolini, C.; Kenny, J. M. *Chem. Phys. Lett.* **2004**, 383, 617.
- (44) Dresselhaus, M. S.; Dresselhaus, G.; Sugihara, K.; Spain, I. L.; Goldberg H. A. *Graphite Fibers and Filaments*; Springer Series in Materials Science 5; Springer-Verlag: New York, 1988.